IRAQI JOURNAL OF MATERIALS
Volume (4) Issue (4) October-December 2025, pp. 205-210

Second Harmonic Generation of Polymorphic Bismuth Halide Structures

Manga D. Awanta, Sigame F. Yukane, Noyaga L. Memereke

Department of Electronic Engineering, Faculty of Engineering, University of Bangui, CENTRAL AFRICAN REPUBLIC

Abstract
In this work, synthesis and utilization of hybrid materials from the Et_3NH^+, Bi^{3+}, and Br^- components for second harmonic generation (SHG) are presented. Two different phases that both had the exact same chemical composition, $(Et_3NH)_3Bi_2Br_9$, were crystallized. These two phases were noteworthy because they possessed contrasting crystal structures: one phase was noncentrosymmetric and could generate an SHG signal, while the other phase was centrosymmetric and lacked SHG capability.

Keywords: Second harmonic generation; Bismuth halide; Polymorphism; Noncentrosymmetric phase
Received: 6 September 2025; **Revised:** 27 September; **Accepted:** 30 September; **Published:** 1 October 2025

1. Introduction

Second Harmonic Generation (SHG) is a pivotal concept in **nonlinear optics** and stands as a powerful, non-invasive analytical technique with far-reaching applications across physics, materials science, and biology [1]. Discovered shortly after the invention of the laser, SHG involves the conversion of two photons of the same frequency (ω) into a single photon with exactly twice the frequency (2ω) and, consequently, half the wavelength [2-4]. This frequency doubling process is a second-order nonlinear optical effect, which means it only occurs when matter interacts with an intense electric field, typically from a high-intensity, pulsed laser [5]. The importance of SHG stems primarily from its intrinsic sensitivity to symmetry and its utility as a label-free, non-destructive probe for structure and interfaces [6].

The critical significance of second harmonic generation (SHG) lies in the fundamental conditions required for its occurrence. First, the sensitivity to non-centrosymmetric structure as the defining feature of SHG is its dependence on the second-order nonlinear susceptibility tensor ($\chi^{(2)}$) of a material [7,8]. A non-zero $\chi^{(2)}$ is only possible in a medium that lacks an inversion center (i.e., a non-centrosymmetric material) [9,10]. SHG is strictly forbidden (at the electric-dipole level) in materials with inversion symmetry, such as common gases, liquids, and many crystalline solids (e.g., cubic crystals) [11]. Therefore, the presence of a strong SHG signal immediately indicates that the probed material possesses a specific polar, non-centrosymmetric crystalline or molecular structure (like quartz, certain ferroelectrics, or biological polymers) [12]. Even in materials that are centrosymmetric in the bulk, the symmetry is broken at the surface or interface. This inherent symmetry-breaking allows SHG to be generated exclusively from this boundary region. This makes SHG an exceptionally powerful, non-optical technique for studying the structure, molecular orientation, and dynamics of a single-molecule layer at any interface (e.g., solid/gas, liquid/liquid, or buried solid/solid interfaces), providing interface specificity that linear optical methods cannot match [13]. Second, the coherent and instantaneous signal. SHG is a coherent process, meaning the generated light maintains a fixed phase relationship with the incident light [14]. It is also an instantaneous process as it does not involve the population of a real excited state (it uses a virtual state) [15]. Unlike fluorescence techniques, which rely on absorbing energy and then re-emitting it, SHG conserves energy and does not involve the transfer of energy to the material's internal degrees of freedom. This characteristic makes SHG an ideal, non-damaging probe for sensitive samples like living biological tissue, as it causes no photobleaching and minimal phototoxicity [16,17].

The unique properties of SHG have led to its diverse deployment in both fundamental research and industrial technology [18]. The original and perhaps most widespread industrial application of SHG is in laser frequency doubling to produce coherent light at wavelengths that are difficult or impossible to generate directly [19]. The most common example is the generation of 532 nm green laser light from a 1064 nm near-infrared Nd:YAG laser. The infrared beam is passed through a nonlinear crystal (such as KTP, BBO, or LBO) under strict phase-matching conditions to efficiently convert the light [20,21]. SHG

is also used to produce UV and deep-UV light by frequency-doubling visible light, a necessary process for applications in photolithography, precision material processing, and advanced spectroscopy [22].

The second harmonic generation microscopy (SHGM) has become an indispensable, label-free imaging modality in biomedicine, offering high-resolution, three-dimensional (3D) visualization of specific biological structures [23]. SHGM selectively highlights endogenous biomolecules, such as collagen and myosin that naturally possess non-centrosymmetric structures [24,25]. Also, the surface-specificity of SHG is exploited to characterize both bulk materials and engineered structures. SHG serves as a unique optical probe for phenomena occurring at interfaces [26,27]. In materials science, SHG is essential for determining the crystal lattice symmetry and orientation of thin films, low-dimensional materials (like monolayer TMDs), and ferroelectric domains [28]. Polarization-resolved SHG, where the polarization of the input and output light is systematically varied, allows for the precise mapping of $\chi^{(2)}$ tensor components to determine structural symmetry and strain. SHG is a vital tool for studying defects in semiconductors, grain boundaries in 2D materials, and the properties of plasmonic nanoparticles, which often exhibit enhanced SHG due to localized surface plasmon resonances [29,30].

In this work, synthesis and utilization of hybrid materials from the Et_3NH^+, Bi^{3+}, and Br^- components for second harmonic generation (SHG) were presented. Two different phases that both had the exact same chemical composition, $(Et_3NH)_3Bi_2Br_9$, were crystallized. These two phases were noteworthy because they possessed contrasting crystal structures: one phase was noncentrosymmetric and could generate an SHG signal, while the other phase was centrosymmetric and lacked SHG capability.

2. Experimental Part

Two distinct crystalline phases (polymorphs) of $(Et_3NH)_3Bi_2Br_9$ were synthesized via evaporation of aqueous solutions. Bismuth(III) oxide and triethylamine were dissolved in hydrobromic acid (HBr). A triclinic phase (noncentrosymmetric) phase-pure sample was obtained via slow evaporation at room temperature. This phase, crystallizing in the P1 space group, could be grown into large, high-quality crystals (up to 4–5 mm). A mixture of the triclinic and monoclinic (P21/c space group) phases was obtained through rapid evaporation in an oven at 95°C. Solid solutions of $(Et_3NH)_3(Bi_{1-x}Sb_x)_2Br_9$ were also synthesized, forming in the triclinic phase across the entire concentration range ($0 \le x \le 1$). Both phases are built from isolated noncentrosymmetric $[Bi_2Br_9]^{3-}$ dimeric units. The structural difference stems from how these units are arranged: they are almost perfectly coaligned in the noncentrosymmetric triclinic phase and related by an inversion center in the centrosymmetric monoclinic phase.

Thermal analysis (DSC and TGA) on the triclinic phase showed multiple phase transitions and a low melting point at 135°C. This low melting point enabled melt processing, a rare technique for hybrid materials. Slow cooling of the melt resulted in the pure triclinic phase, while fast cooling or quenching produced a mixture, highlighting thermodynamic control for the triclinic phase and kinetic control for the metastable monoclinic phase. Second Harmonic Generation (SHG) measurements were performed on the noncentrosymmetric triclinic phase using 2090 nm (IR) and 1064 nm (Visible/NIR) laser excitation sources.

3. Results and Discussion

The powder X-ray diffraction (PXRD) pattern shown in Fig. (1) for the $(Et_3NH)_3Bi_2Br_9$ compound reveal the formation of two distinct polymorphs, depending on the crystallization conditions. The method of evaporation controls which crystal structure is predominantly formed and, consequently, the resulting XRD pattern. Slow evaporation at room temperature results in a phase-pure sample of the triclinic phase of $(Et_3NH)_3Bi_2Br_9$. The triclinic phase has a noncentrosymmetric structure, belonging to the P1 space group. This phase is favored under equilibrium conditions and can be obtained as large, high-quality crystals. Rapid evaporation at 95°C yields a mixture of the triclinic and monoclinic polymorphs of $(Et_3NH)_3Bi_2Br_9$. The monoclinic phase is centrosymmetric, belonging to the P21/c space group. The monoclinic phase is considered metastable at room temperature, forming under non-equilibrium, fast-crystallization processes. The XRD was also crucial in demonstrating the temperature-assisted phase conversion between the two polymorphs, which is possible due to the compound's relatively low melting point (~130°C for the Bi phase). Slow cooling of a molten mixture of the two polymorphs from 150°C back to room temperature results in a pattern corresponding to the phase-pure triclinic polymorph. Fast cooling rates or quenching of the melt (even when starting with a pure triclinic sample) leads to a PXRD pattern that shows a mixture of the triclinic and monoclinic phases. Accordingly, the PXRD patterns serve as the primary tool for identifying and distinguishing the noncentrosymmetric triclinic phase from the centrosymmetric monoclinic phase and confirming their interconvertibility by controlling the evaporation/cooling rate.

ISSN (print) 2958-8960 (online) 3006-6042 Printed in IRAQ

Figure (2) displays differential scanning calorimetry (DSC) data, which measures the variation of heat flow with temperature for the hybrid bismuth/antimony halide solid solutions, $(Et_3NH)_3(Bi_{1-x}Sb_x)_2Br_9$, specifically comparing the pure Bi phase (x=0) and the pure Sb phase (x=1). The DSC analysis primarily reveals the thermal behavior of these materials, including phase transitions and melting points. Endothermic peaks (downward deflections in the heat flow) correspond to processes that absorb heat, such as phase transitions and melting. The figure show distinct endothermic events: phase transitions (low temperature) and melting point (high temperature). In the first event, the Bi phase $(Et_3NH)_3Bi_2Br_9$ exhibits multiple endothermic peaks corresponding to polymorphic phase transitions. The main transitions occur at onset temperatures of approximately 90°C, 97°C, and 115°C. The Sb phase $(Et_3NH)_3Sb_2Br_9$ also shows a series of phase transitions, but they occur at significantly lower temperatures compared to the Bi phase. In the second event, the final, largest endothermic peak corresponds to the melting point (T_m). The Bi phase melts at an onset temperature of approximately 135°C. The Sb phase melts at a much lower temperature of approximately 75°C. The comparison clearly shows that substituting Bi with the smaller Sb ion in the solid solution leads to a nonlinear decrease in the temperature of all phase transitions, including the melting point. This decrease is generally attributed to the difference in ionic radii (Sb^{3+} is 0.76Å vs. Bi^{3+} is 1.03Å). The low melting points for both compounds, particularly the Bi phase at 135°C, make them candidates for melt-processable materials. The extremely low melting point of the pure antimony compound (75°C) suggests that it may function as an ionic liquid. The multiple transitions observed in the Bi phase confirm its rich structural and temperature polymorphism.

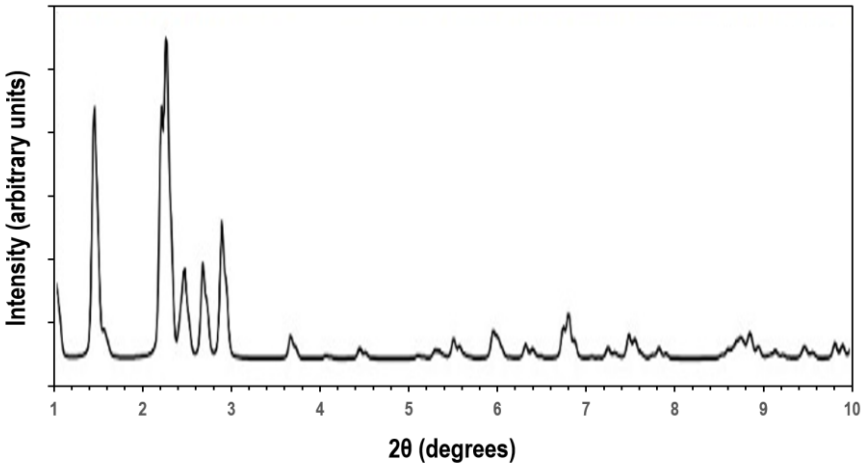

Fig. (1) PXRD pattern of $(Et_3NH)_3Bi_2Br_9$ prepared in this work

Figure (3) presents the thermogravimetric analysis (TGA) data, showing the variation of weight loss as a function of temperature for the hybrid bismuth/antimony halide solid solutions, $(Et_3NH)_3(Bi_{1-x}Sb_x)_2Br_9$, specifically comparing the pure Bi phase (x=0) and the pure Sb phase (x=1). The TGA curves track the thermal stability and decomposition behavior of the materials. A sharp drop in the weight percentage indicates the thermal decomposition or volatilization of the compound. Both the Bi phase and the Sb phase show excellent thermal stability up to their respective decomposition temperatures. The weight remains at 100% until the compounds begin to break down. This stability is important for any device application, confirming the material won't degrade under ambient or slightly elevated operating temperatures. The material begins to decompose at a relatively high temperature, with the initial significant weight loss starting around 200°C. The decomposition proceeds through a series of steps. The Sb phase (x=1) shows a slightly lower onset of decomposition, starting around 190°C. The sharp, steep weight loss observed for both compounds indicates rapid and complete thermal degradation. This rapid loss is characteristic of the volatilization of the organic component (the triethylammonium cation, Et_3NH^+) and the resulting decomposition of the inorganic framework. The overall TGA profile confirms that the materials decompose before the temperature reaches approximately 300°C, confirming they are not stable at very high processing temperatures but are stable well above their melting points (which were found to be 135°C and 75°C for the Bi and Sb phases, respectively). Consequently, the TGA

ISSN (print) 2958-8960 (online) 3006-6042 Printed in IRAQ

curves demonstrate that these hybrid materials are thermally robust up to approximately 200◦C but undergo complete decomposition shortly thereafter, limiting their use in high-temperature applications.

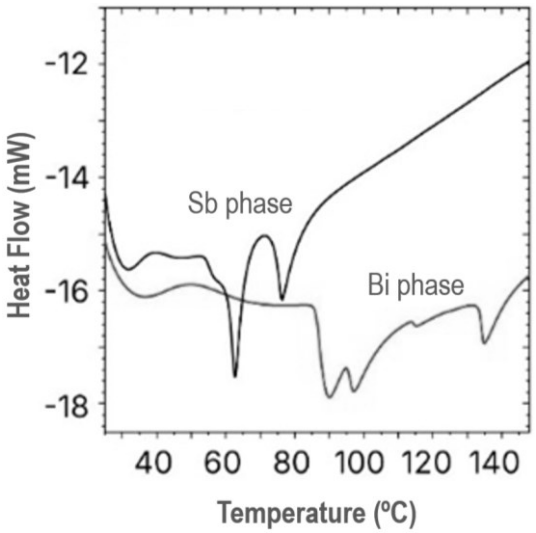

Fig. (2) Variation of heat flow with temperature for the multi=component $(Et_3NH)_3(Bi_{1-x}Sb_x)_2Br_9$ prepared in this work

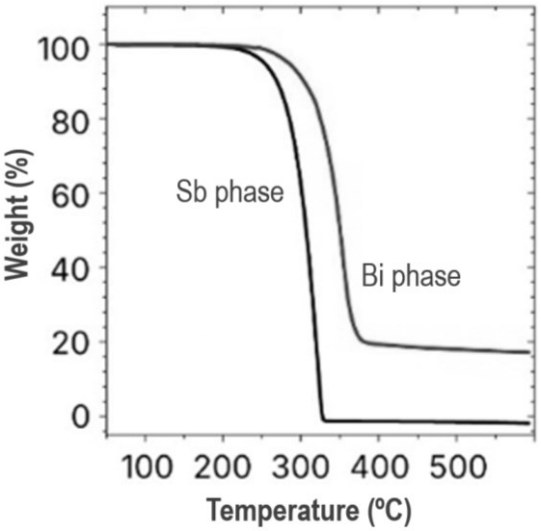

Fig. (3) Variation of weight with temperature for the multi-component $(Et_3NH)_3(Bi_{1-x}Sb_x)_2Br_9$ prepared in this work

Figure (4) illustrates the second harmonic generation (SHG) response of the noncentrosymmetric triclinic phase of $(Et_3NH)_3Bi_2Br_9$ powder, comparing its intensity to the commercial standard AGS crystal across various particle sizes. The data reveals critical differences in the material's nonlinear optical performance and phase-matching behavior. The $(Et_3NH)_3Bi_2Br_9$ phase exhibits a relatively weak SHG signal, with its maximum intensity being only about 0.08 times that of AGS. AGS is an established mid-infrared nonlinear optical material, meaning the Bi-halide's intrinsic nonlinearity is much lower than this commercial standard in the IR region. The most significant feature is the clear dependence of the SHG intensity on particle size. As the average particle size increases from 53 μm to 180 μm, the SHG intensity generally increases or plateaus (it does not fall). This behavior is the definitive signature of phase-matchable SHG. Phase matching is the condition where the fundamental and harmonic waves travel at the same speed (or maintain a constant relative phase) through the crystal, allowing the SHG signal to accumulate coherently over longer crystal lengths (i.e., larger particles). This confirms that the triclinic $(Et_3NH)_3Bi_2Br_9$ possesses sufficient birefringence to satisfy the phase-matching condition for 2090 nm fundamental light.

Figure (5) compares the SHG intensity generated $(Et_3NH)_3Bi_2Br_9$ phase to KDP crystal. The SHG intensity is measured to be significantly higher in absolute terms than the signal compared to AGS

 ISSN (print) 2958-8960 (online) 3006-6042 Printed in IRAQ

crystal. However, the chart is normalized to a different material. Crucially, the SHG intensity shows a clear and rapid decrease as the particle size increases. The intensity is highest for the smallest particles (53 μm) and drops significantly for the largest ones. This indicates non-phase-matchable SHG. Without phase matching, the SHG signal generated in different regions of the crystal lattice dephases (interferes destructively) over the propagation length. Therefore, the signal accumulation is limited by the coherence length of the material, not the particle size, leading to the observed drop in signal for larger particles.

The stark difference in phase-matching behavior highlights the strong wavelength-dependent optical properties of the triclinic $(Et_3NH)_3Bi_2Br_9$. The material is phase-matchable in the mid-IR range (2090 nm fundamental), making it a candidate for mid-IR frequency conversion, though its efficiency is low relative to AGS. The compound is not phase-matchable at 1064 nm. This is likely due to increased dispersion (difference in refractive index) between the fundamental (1064 nm) and harmonic (532 nm) waves near the material's bandgap of 2.6 eV. The SHG response itself is entirely attributable to the material's noncentrosymmetric triclinic crystal structure, which ensures a non-zero second-order nonlinear susceptibility tensor ($\chi^{(2)}$). The different arrangements of the noncentrosymmetric $[Bi_2Br_9]^{3-}$ units are responsible for this essential property.

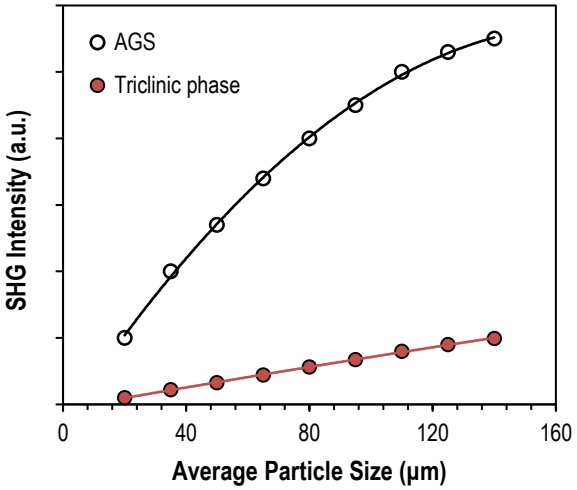

Fig. (4) Variation of SHG intensity with average particle size for the triclinic phase $(Et_3NH)_3(Bi_{1-x}Sb_x)_2Br_9$ compared to AGS crystal

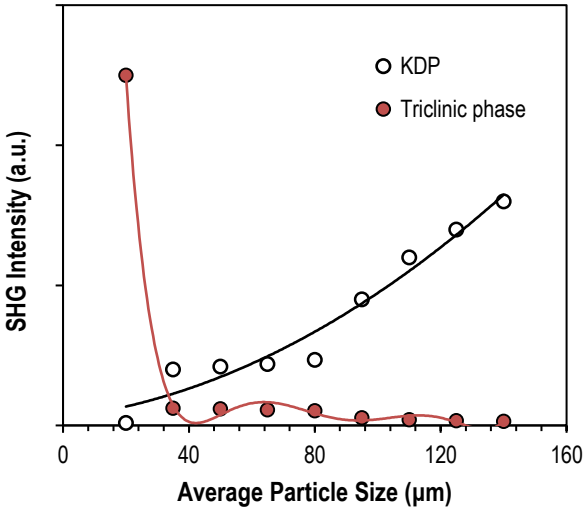

Fig. (5) Variation of SHG intensity with average particle size for the triclinic phase $(Et_3NH)_3(Bi_{1-x}Sb_x)_2Br_9$ compared to KDP crystal

ISSN (print) 2958-8960 (online) 3006-6042 Printed in IRAQ

4. Conclusion

In this work, synthesis and utilization of hybrid materials from the Et_3NH^+, Bi^{3+}, and Br^- components for second harmonic generation (SHG) are presented. Two different phases that both had the exact same chemical composition, $(Et_3NH)_3Bi_2Br_9$, were crystallized. These two phases were noteworthy because they possessed contrasting crystal structures: one phase was noncentrosymmetric and could generate an SHG signal, while the other phase was centrosymmetric and lacked SHG capability.

References

[1] A. Kehrer, S.-q Dou, and A. Weiss, "79,81Br−127I−NQR, and Crystal Structure of Glycyl-l-alanine Hydrobromide Monohydrate and Hydroiodide Monohydrate", *Z. Naturforsch. A,* 44 (1989) 659-668.
[2] P.R. Tulip and S.P. Bates, "First principles determination of structural, electronic and lattice dynamical properties of a model dipeptide molecular crystal", *Mol. Phys.,* 107 (2009) 2201-2212.
[3] P. Tzankov and V. Petrov, "Effective second-order nonlinearity in acentric optical crystals with low symmetry", *Appl. Opt.,* 44 (2005) 6971-6985.
[4] H. Wang and A.M. Weiner, "Efficiency of short-pulse type-I second-harmonic generation with simultaneous spatial walk-off, temporal walk-off, and pump depletion", *IEEE J. Quantum Electron.,* 39 (2003) 1600-1618.
[5] S.D. Stranks et al., "Electron-Hole Diffusion Lengths Exceeding 1 Micrometer in an Organometal Trihalide Perovskite Absorber", *Science,* 342 (2013) 341-344.
[6] M. Liu, M.B. Johnston, and H.J. Snaith, "Efficient Planar Heterojunction Perovskite Solar Cells by Vapour Deposition", *Nature,* 501 (2013) 395-398.
[7] J.-H. Im et al.; "Growth of $CH_3NH_3PbI_3$ Cuboids with Controlled Size for High-Efficiency Perovskite Solar Cells", *Nat. Nanotechnol.,* 9 (2014) 927-932.
[8] H. Zhou et al., "Interface Engineering of Highly Efficient Perovskite Solar Cells", *Science*, 345 (2014) 542-546.
[9] W.S. Yang et al., "High-Performance Photovoltaic Perovskite Layers Fabricated Through Intramolecular Exchange", *Science,* 348 (2015) 1234-1237.
[10] Z.-K. Tan et al., "Bright Light-Emitting Diodes Based on Organometal Halide Perovskite", *Nat. Nanotechnol.,* 9 (2014) 687-692.
[11] J.C. Yu et al., "High-Performance Planar Perovskite Optoelectronic Devices: A Morphological and Interfacial Control by Polar Solvent Treatment", *Adv. Mater.,* 27 (2015) 3492-3500.
[12] J. Wang et al., "Interfacial Control Toward Efficient and Low-Voltage Perovskite Light-Emitting Diodes", *Adv. Mater.,* 27 (2015) 2311-2316.
[13] G. Li et al., "Efficient Light-Emitting Diodes Based on Nanocrystalline Perovskite in a Dielectric Polymer Matrix", *Nano Lett.,* 15 (2015) 2640-2644.
[14] H. Cho et al., "Overcoming The Electroluminescence Efficiency Limitations Of Perovskite Light-Emitting Diodes", *Science,* 350 (2015) 1222-1225.
[15] M. Yuan et al., "Perovskite Energy Funnels For Efficient Light-Emitting Diodes", *Nat. Nanotechnol.,* 11 (2016) 872-877.
[16] N. Wang et al., "Perovskite Light-Emitting Diodes Based on Solution-Processed Self-Organized Multiple Quantum Wells", *Nat. Photon.,* 10 (2016) 699-704.
[17] Z. Xiao et al., "Efficient Perovskite Light-Emitting Diodes Featuring Nanometre-Sized Crystallites", *Nat. Photon.,* 11 (2017) 108-115.
[18] L. Zhang et al., "Ultra-Bright and Highly Efficient Inorganic Based Perovskite Light-Emitting Diodes", *Nat. Commun.,* 8 (2017) 15640.
[19] S.D. Stranks and H.J. Snaith, "Metal-Halide Perovskites For Photovoltaic And Light-Emitting Devices", *Nat. Nanotechnol.,* 10 (2015) 391-402.
[20] S.D. Stranks, "Nonradiative Losses in Metal Halide Perovskites", *ACS Energy Lett.,* 2 (2017) 1515-1525.
[21] F. Zhang et al., "Brightly Luminescent and Color-Tunable Colloidal $CH_3NH_3PbX_3$ (X = Br, I, Cl) Quantum Dots: Potential Alternatives for Display Technology", *ACS Nano,* 9 (2015) 4533-4542.
[22] F. Deschler et al., "High Photoluminescence Efficiency and Optically Pumped Lasing in Solution-Processed Mixed Halide Perovskite Semiconductors", *J. Phys. Chem. Lett.,* 5 (2014) 1421-1426.
[23] J.C. Yu et al., "High-Performance Perovskite Light-Emitting Diodes *via* Morphological Control of Perovskite Films", *Nanoscale,* 8 (2016) 7036-7042.
[24] A. Sadhanala et al., "Electroluminescence from Organometallic Lead Halide Perovskite-Conjugated Polymer Diodes", *Adv. Electron. Mater.,* 1 (2015) 1500008.
[25] J. Li et al., "Single-Layer Halide Perovskite Light-Emitting Diodes with Sub-Band Gap Turn-On Voltage and High Brightness", *J. Phys. Chem. Lett*., 7 (2016) 4059-4066.
[26] X. Zhang et al., "All-Inorganic Perovskite Nanocrystals for High-Efficiency Light Emitting Diodes: Dual-Phase $CsPbBr_3$-$CsPb_2Br_5$ Composites", *Adv. Funct. Mater.,* 266 (2016) 4595-4600.
[27] Z. Chen et al., "High-Performance Color-Tunable Perovskite Light Emitting Devices through Structural Modulation from Bulk to Layered Film", *Adv. Mater.,* 29 (2017) 1603157.
[28] B.R. Lee et al., "Highly Efficient Polymer Light-Emitting Diodes Using Graphene Oxide as a Hole Transport Layer", *ACS Nano,* 6 (2012) 2984-2991.
[29] H. Choi et al., "Conjugated Polyelectrolyte Hole Transport Layer For Inverted-Type Perovskite Solar Cells", *Nat. Commun.,* 6 (2015) 7348.
[30] J.-M. Yun et al., "Solution-Processable Reduced Graphene Oxide as a Novel Alternative to PEDOT:PSS Hole Transport Layers for Highly Efficient and Stable Polymer Solar Cells", *Adv. Mater.,* 23 (2011) 4923-4928.

 ISSN (print) 2958-8960 (online) 3006-6042 Printed in IRAQ